Hybrid LVRT Control of Doubly-Fed Variable Speed Pumped Storage to Shorten Crowbar Operational Duration

Donghai Zhu, *Senior Member, IEEE*, Zhen Wang, Yumei Ma, *Student Member, IEEE*, Jiabing Hu, *Senior Member, IEEE*, Xudong Zou, *Member, IEEE*, and Yong Kang, *Fellow, IEEE*

***Abstract*—Crowbar is the most widely used low voltage ride-through (LVRT) solution for doubly-fed variable speed pumped storage (VSPS) unit. However, the conventional crowbar solution suffers from excessive crowbar activation period when applied to large-scale VSPS unit, which leads to the disadvantages of high reactive power absorption and huge electromagnetic torque oscillation. To solve the issue, this article analyzes the condition of crowbar release from the perspective of system controllability. Based on it, a hybrid LVRT control strategy combining crowbar and dynamic demagnetizing control is proposed. In this strategy, the crowbar operational duration can be minimized by optimizing the demagnetizing coefficient dynamically. Moreover, the objective of reactive power support or electromagnetic torque oscillation suppression can be achieved to enhance the transient performance of VSPS unit. Finally, the proposed hybrid LVRT control method is validated by the experiments.**

***Index Terms*—Crowbar, doubly-fed variable-speed pumped storage unit, low voltage ride through control.**

I. Introduction

With large-scale renewable energy connected to the power grid, the unpredictable and intermittent behavior of renewable energy can lead to fluctuations in power generation, resulting in uncontrollable variations in power supply [1], [2]. To resolve the fluctuation issue in power and frequency, the variable speed pumped storage (VSPS) has been a promising solution due to its advantages of rapidity in power regulation, strong flexibility and reliability. Different from the traditional fixed-speed unit, the feature of VSPS is that its speed can be regulated to match a wider range of water heads and improve operating efficiency. Owing to this characteristic, the VSPS is quite adapted to be employed at sites having wide water head variations through variable speed operation, making it gradually gain a large number of applications worldwide [3], [4].

Currently, there are two main strategies for pumped storage units to realize variable speed operation: the doubly-fed induction machine (DFIM) scheme and the converter-fed synchronous machine (CFSM) scheme [5], [6]. Generally, due to the fatal drawback of requiring a full-rated converter, the CFSM scheme is not feasible for high-power applications (>100 MW) [7], [8]. The doubly-fed VSPS units are preferred for large power plants (e.g., Fengning Pumped Storage Power Station in Hebei Province of China) [9], since the DFIM scheme only requires a part-load excitation converter. However, the stator of the doubly-fed VSPS unit is directly connected to the grid, it is sensitive to grid voltage disturbance. When a grid fault occurs, the rotor-side converter (RSC) is prone to suffering from overcurrent, which may trip the whole system and result in the failure of the LVRT [10], [11].

At present, there is still a paucity of research on the low voltage ride-through (LVRT) issue in doubly-fed VSPS. In industry, most of the operated units from manufacturers use the crowbar circuit as the LVRT solution [12], [13]. It offers a series of advantages such as the capability to ride through severe grid fault, simple structure, and low-cost, which has been widely used in doubly-fed wind turbine [14], [15], [16]. However, the crowbar also introduces some disadvantages, which will be significantly magnified in the doubly-fed VSPS. On the one hand, once the crowbar is activated, VSPS will absorb reactive power from grid. Due to the large capacity of the VSPS, the operation of power grid will be worsened [17]. On the other hand, the transient time constant of VSPS is typically 4-5 times longer than that of doubly-fed wind turbine [18], resulting in significantly prolonged crowbar activation and persistent torque oscillation. As crowbar activation time increases, the VSPS has the challenge in supplying rapid reactive support and suppressing torque oscillation during grid fault.

To address the disadvantages of crowbar, some solutions are proposed in DFIG-based wind turbines to fulfill the LVRT requirement by improving control strategy for RSC. In terms of direct rotor overcurrent suppression, Lima et al. [19] proposed a stator current feedback control method, where the measured stator current is directly adopted as the rotor current references. Xiao et al. [20] proposed a flux tracking control to replace the current control for the fault current suppression. In order to

Manuscript received 31 March 2024; revised 23 June 2024; accepted 24 July 2024. Date of publication 29 July 2024; date of current version 11 September 2024. This work was supported by the National Natural Science Foundation of China under Grant 52225704. Recommended for publication by Associate Editor: Y. Du. *(Corresponding author: Zhen Wang.)*

The authors are with the State Key Laboratory of Advanced Electromagnetic Technology, School of Electrical and Electronic Engineering, Huazhong University of Science and Technology, Wuhan 430074, China (e-mail: zhudh@hust.edu.cn; wangzhen21@hust.edu.cn; maym@hust.edu.cn; j.hu@hust.edu.cn; xdzou@mail.hust.edu.cn; ykang@mail.hust.edu.cn).

Color versions of one or more figures in this article are available at https://doi.org/10.1109/TPEL.2024.3435063.

Digital Object Identifier 10.1109/TPEL.2024.3435063

reduce the rotor voltage requirement and attenuate the stator flux, Ran et al. [21], Shen et al. [22], and Hu et al. [23] proposed a series of demagnetization controls to inject certain components related to stator flux into the rotor current. Huang et al. [24] and Zhu et al. [25] proposed the scaled current tracking control to demagnetize and avoid the use of flux observation. In [26], an inductance-emulating control is proposed to compromise the rotor voltage requirement and fault current. In addition, for VSPS units, Bidgoli et al. [27] proposed an advanced vector control to improve LVRT capability in both generation and motor modes. By switching the control algorithm to the synchronization one, the method proposed in [28] can eliminate rotor and stator overcurrent. The above control methods can assist the VSPS unit with LVRT effectively under light grid fault. However, under severe grid fault, limited by the converter capacity, these methods struggle to maintain unit controllability, leading to the failure of LVRT. Particularly, the capability of VSPS unit's converter (0.1–0.2 p.u.) is typically lower than wind turbine (0.3–0.4 p.u.), which further weakens the LVRT capability of above methods. Thus, when a severe grid fault occurs, the crowbar activation cannot be avoided in VSPS unit.

To discard the defects of the aforementioned two types of technologies, Lopez et al. [29] proposed a strategy combining the crowbar and the demagnetizing technique to shorten the crowbar activation period and maintain the severe LVRT capability, which is an effective solution. Unfortunately, Lopez et al. [29] does not concern the effect of the demagnetizing coefficient, which results in this combined method still suffers from the excessive crowbar activation period when applied in VSPS. In short, for VSPS units, the existing LVRT methods are still insufficient to avoid prolonged crowbar activation under severe grid fault. To cope with it, inspired by [29], this article proposes a hybrid LVRT control combining dynamic demagnetization and crowbar to minimize the crowbar operational duration in doubly-fed VSPS. The proposed method dynamically optimizes the demagnetization coefficient during crowbar activation period to minimize the crowbar operational duration, and further improves the transient performance by injecting additional positive-sequence current after the crowbar release. The main contributions of this article are summarized as follows.

1) The transient characteristics of VSPS unit with crowbar are analyzed, and the crowbar release condition are presented from the perspective of system controllability.
2) A hybrid LVRT control is proposed. Implementing this method, the crowbar is activated briefly and the converter can resume operation rapidly.
3) The effect of positive sequence current on the transient characteristics is analyzed. Based on it, the transient control objectives of reactive power support and torque oscillation suppression are realized, respectively.

The rest of this article is organized as follows. In Section II, the transient characteristics of VSPS with crowbar and the crowbar release condition are analyzed. In Section III, the principle and design of the proposed LVRT control strategy are presented. Afterward, in Sections IV, the HIL experiment results are presented to validate the effectiveness of the proposed method. Finally, Section V concludes this article.

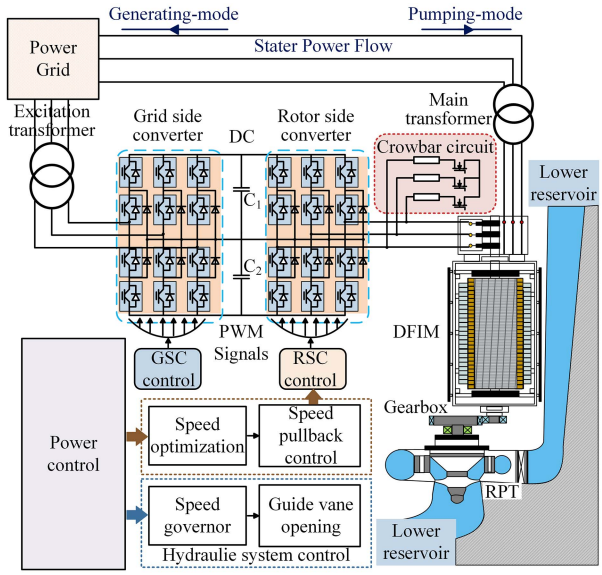

Fig. 1. Structure of doubly-fed VSPS.

II. Transient Characteristics Analysis of VSPS With Crowbar Circuit

A. VSPS Model

Fig. 1 shows the main structure of doubly-fed VSPS. It is observable that the reversible pump-turbine (RPT) and DFIM are connected through a gearbox, the rotor winding of DFIM is connected with a multilevel back-to-back (BTB) converter. The stator of DFIM is directly connected to grid through the main transformer and grid side converter (GSC) connected to the power grid through an excitation transformer [30]. The power output of VSPS is indirectly controlled by the speed governor through adjusting the opening of guide vane, while the speed is directly controlled by the converter.

Based on the structure of doubly-fed VSPS, the VSPS system can be divided into two main systems, namely the excitation system (composed of DFIM and BTB converter) and hydraulic system (composed of speed governor and RPT). Under grid fault, the transient process is fairly fast with an electromechanical transient time scale (milliseconds), while the response speed of the hydraulic subsystem is relatively slow (seconds). Therefore, within the electromechanical transient time scale, the model in this article is established on DFIM [31].

To facilitate the analysis, the motor convention is adopted for stator and rotor sides, and all variables are referred to the stator side. In the stationary reference frame, the equations of DFIM's voltage and flux can be expressed as [32]

$$\begin{cases} \boldsymbol{U}_s^s = R_s \boldsymbol{I}_s^s + \frac{d}{dt}\boldsymbol{\psi}_s^s \\ \boldsymbol{U}_r^r = R_r \boldsymbol{I}_r^r + \frac{d}{dt}\boldsymbol{\psi}_r^r \end{cases} \tag{1}$$

$$\begin{cases} \boldsymbol{\psi}_s^s = L_s \boldsymbol{I}_s^s + L_m \boldsymbol{I}_r^s \\ \boldsymbol{\psi}_r^r = L_m \boldsymbol{I}_s^r + L_r \boldsymbol{I}_r^r \end{cases} \tag{2}$$

where $\boldsymbol{U}$, $\boldsymbol{I}$, and $\boldsymbol{\psi}$ are the vectors of voltage, current, and flux, respectively. L and R are the inductance and resistance. L_m is the magnetizing inductance. Superscripts "s" and "r" denote the

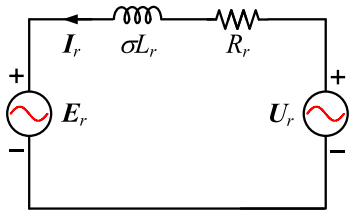

Fig. 2. Equivalent circuit of DFIM viewed from the rotor-side.

stator- and rotor-reference frames, respectively. Subscripts "s" and "r" denote the stator- and rotor-side variables, respectively.

Substituting (1) into (2), yields

$$\boldsymbol{U}_r^r = \underbrace{\frac{L_m}{L_s}\frac{d\boldsymbol{\psi}_s^r}{dt}}_{\boldsymbol{E}_r} + \underbrace{\left(R_r + \sigma L_r \frac{d}{dt}\right)\boldsymbol{I}_r^r}_{\boldsymbol{U}_{RL}} \tag{3}$$

where $s = 1 - L_{\mathrm{m}}^2/L_s L_r$ is the leakage coefficient. σL_r is the rotor transient inductance. $\boldsymbol{E}_r$ is the electromotive force (EMF). $\boldsymbol{U}_{RL}$ is the voltage dip on rotor impedance (i.e., σL_r and R_r).

Then, the equivalent circuit of DFIM can be obtained [32], as illustrated in Fig. 2.

B. Transient Characteristic Analysis

As shown in Fig. 2, rotor current can be regarded as a result of EMF $\boldsymbol{E}_r$ and RSC's output voltage $\boldsymbol{U}_r$. During normal operation, the stator flux rotates at synchronous speed, meanwhile, the flux rotates at slip speed. Therefore, the amplitude of EMF is proportional to the slip and can be approximated as

$$E_{\mathbf{r}} = \frac{L_{\mathrm{m}}}{L_{\mathrm{s}}}\psi_{\mathrm{s}}\omega_{\mathrm{s}}s \approx U_{\mathrm{s}}s \tag{4}$$

where ω_s is the synchronous speed. U_s is the rated stator voltage. $s = (\omega_s - \omega_r)/\omega_s$ is the slip, and $s \in [-0.1, 0.1]$. ω_r is rotor speed.

According to (4), it can be obtained that the EMF under normal condition cannot exceed 10% of the rated stator voltage. Since the maximum output voltage of RSC is generally taken as 0.1-0.2U_s, according to (4), it is apparent that the rotor current can be completely controlled by U_r under normal condition.

When a symmetrical fault occurs at time $t = 0$, the stator flux will contain certain natural component ψ_{sn}, and its initial amplitude can be expressed as

$$\psi_{sn}(t=0) = \frac{hU_s}{j\omega_{\mathrm{s}}} \tag{5}$$

where h is the depth of grid voltage dip.

Since the natural component of stator flux will stop rotating, its rotate speed with respect to the rotor windings becomes ω_r. As a result, the initial amplitude of EMF becomes

$$E_r(t=0) = \underbrace{\frac{L_{\mathrm{m}}}{L_{\mathrm{s}}}U_s \cdot (1-h) \cdot s}_{E_{rp}(t=0)} \underbrace{- \frac{L_{\mathrm{m}}}{L_{\mathrm{s}}}U_s \cdot h \cdot (1-s)}_{E_{rn}(t=0)} \tag{6}$$

where E_{rp} is the positive-sequence component, while E_{rn} is the natural component.

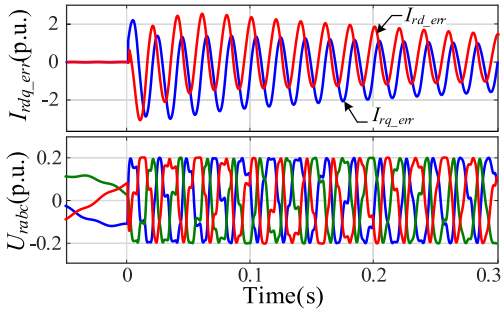

Fig. 3. Rotor current tracking error and RSC's output voltage under fault.

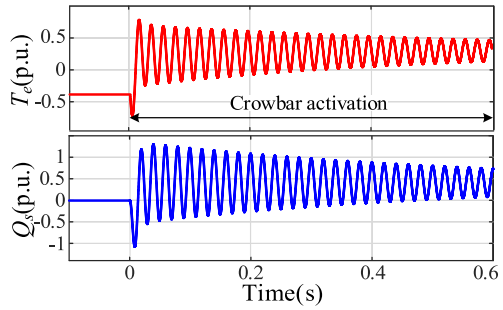

Fig. 4. Electromagnetic torque and reactive power when crowbar is activated.

It can be obtained from (6) that, the natural component is proportional to "1−s". Thus, the postfault EMF is quite large and will far exceed the RSC's maximum output voltage $U_{r\max}$. As the output voltage of RSC cannot match the postfault EMF, the converter saturates and loses control of the rotor current temporarily, which is the source of the large postfault rotor current.

For instance, under severe grid fault, if the control system still adopts conventional power control mode, its corresponding rotor voltage requirement will exceed $U_{r\max}$. Therefore, the converter will be saturated, the significant rotor current tracking error are inevitable, as shown in Fig. 3. The huge rotor current tracking error will result in postfault overcurrent.

C. Crowbar Characteristic and Release Condition Analysis

To protect the converter against the rotor overcurrent, the most common technique to assist VSPS for LVRT is the crowbar protection circuit. However, there are two major disadvantages when activating the crowbar. On the one hand, the electromagnetic torque of the VSPS oscillates greatly during the crowbar activation, which will pose great press on the drive train. On the other hand, the RSC is blocked and VSPS is out of control when the crowbar is activated. Thereby, as shown in Fig. 4, the positive value of reactive power indicates that the VSPS will absorb a large amount of reactive power from grid, thus deteriorating the operation of power "1−s". Thus, to minimize the disadvantages of crowbar activation and meet the reactive power support requirements proposed in the grid codes, the crowbar should be released as early as possible.

Nevertheless, in principle the crowbar should be activated long enough to allow sufficient demagnetization of the rotor

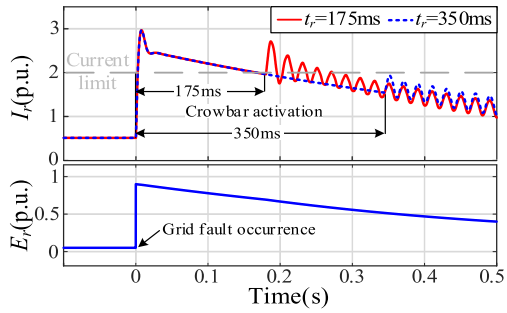

Fig. 5. Rotor current and EMF when crowbar release at 175 ms and 350 ms.

windings and avoid overcurrent [33].When the crowbar activation time is reduced, the remaining undecayed EMF may lead to system out-of-control.

When the crowbar is released, the remaining undecayed EMF can be expressed as follow:

$$\boldsymbol{E}_r^r = \underbrace{s\,(1-h)\,\frac{L_m}{L_s}U_s e^{js\omega_s t_r}}_{\boldsymbol{E}_{rp}} \underbrace{-(1-s)\,h\,\frac{L_m}{L_s}U_s e^{-j\omega_r t_r} e^{-t_r/\tau_c}}_{\boldsymbol{E}_{rn}} \tag{7}$$

where τ_c is the transient time constant of the stator natural flux when crowbar is activated. The crowbar is activated at time $t = 0$ and released at time $t = t_r$.

It is obvious from (7) that, the shorter crowbar activation period, the larger remaining EMF, i.e., the unit is more tends to be uncontrolled. To illustrate it, two examples with crowbar release time of t_r = 175 ms and t_r = 350 ms are presented in Fig. 5, respectively. It can be seen that after crowbar release, the larger undecayed EMF results in more inaccurate current tracking (i.e., the uncontrollable behavior), which makes the overcurrent indecipherable and transient control objectives unachievable.

Consequently, in order to decrease the activation duration of the crowbar, it is necessary to maintain the unit controllable under a higher remaining EMF.

III. Proposed Hybrid LVRT Control

A. Basic Principle

As mentioned in Section II, the key to decrease crowbar activation duration is to keep the unit controllable under remaining EMF, i.e., the required RSC output voltage $\boldsymbol{U}_{\mathrm{RSC}}$ when the rotor current tracks current reference $\boldsymbol{I}_r^*$ should be less than the RSC's maximum output voltage. From Fig. 2, it can be derived that $\boldsymbol{U}_{\mathrm{RSC}}$ is expressed as

$$\boldsymbol{U}_{\mathrm{RSC}} = \underbrace{\frac{L_m}{L_s}\frac{d\boldsymbol{\psi}_s^r}{dt}}_{\boldsymbol{E}_r} + \left(R_r + \sigma L_r \frac{d}{dt}\right)\boldsymbol{I}_r^* \tag{8}$$

It is obvious from (8), when the crowbar is released, the amplitude of $\boldsymbol{U}_{\mathrm{RSC}}$ not only depends on the remaining EMF, but also influenced by current reference. Thus, through the design of $\boldsymbol{I}_r^*$, it is able to keep the system controllable under remaining EMF and reduce the activation time of crowbar.

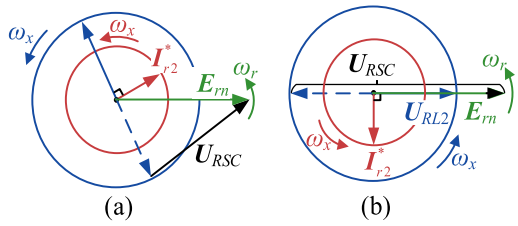

Fig. 6. Vector relationship between $\boldsymbol{U}_{\mathrm{RSC}}$, $\boldsymbol{I}_{r2}^*$, and $\boldsymbol{E}_{rn}$.

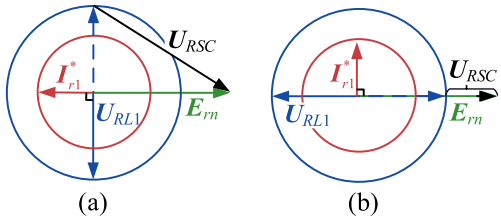

Fig. 7. Vector relationship between $\boldsymbol{U}_{\mathrm{RSC}}$, $\boldsymbol{I}_{r1}^*$, and $\boldsymbol{E}_{rn}$.

On this basis, the effects of different forms of $\boldsymbol{I}_r^*$ on $\boldsymbol{U}_{\mathrm{RSC}}$ need to be evaluated. Since the dominant part of EMF is $\boldsymbol{E}_{rn}$, while the frequency of $\boldsymbol{E}_{rn}$ and $\boldsymbol{\psi}_{sn}$ are fixed as ω_r, the form of the current reference $\boldsymbol{I}_r^*$ can be divided as

$$\boldsymbol{I}_r^* = \boldsymbol{I}_{r2}^* + \underbrace{k_1\boldsymbol{\psi}_{sn} + jk_2\boldsymbol{\psi}_{sn}}_{I_{r1}^*} \tag{9}$$

where $\boldsymbol{I}_{r1}^*$ is the natural component of the current reference with the same frequency as $\boldsymbol{\psi}_{sn}$ (i.e., its frequency is ω_r). k_1 and k_2 are defined as the parallel coefficient and vertical coefficient, respectively. $\boldsymbol{I}_{r2}^*$ is the non-natural component with the frequency of ω_x ($\omega_x \neq \omega_r$).

According to (8), the vector relationship between $\boldsymbol{U}_{\mathrm{RSC}}$, $\boldsymbol{I}_{r2}^*$ and $\boldsymbol{E}_{rn}$ can be illustrated as Fig. 6. From Fig. 6(a) and (b), it can be deduced that due to the different frequencies of $\boldsymbol{I}_{r2}^*$ and $\boldsymbol{E}_{rn}$, the amplitude of $\boldsymbol{U}_{\mathrm{RSC}}$ will oscillate at $(\omega_r - \omega_x)$ frequency, i.e., the rotor voltage requirement will increase. Meanwhile, Fig. 7 shows the vector relationship between $\boldsymbol{U}_{\mathrm{RSC}}$, $\boldsymbol{I}_{r1}^*$ and $\boldsymbol{E}_{rn}$. From Fig. 7(a) and (b), It can be illustrated that the vertical component of $\boldsymbol{I}_{r1}^*$ will increase the rotor voltage requirement, while the parallel component will reduce the rotor voltage requirement.

Furthermore, the amplitude of $\boldsymbol{U}_{\mathrm{RSC}}$ can be expressed as follow:

$$\begin{aligned} U_{\mathrm{RSC}} = {} & |\omega\sigma L_r \boldsymbol{I}_{r2}^*| \\ & + \sqrt{\left(\frac{L_m}{L_s} + k_1\sigma L_r\right)^2 + (k_2\sigma L_r)^2}\,|\omega_r\boldsymbol{\psi}_{sn}| \end{aligned} \tag{10}$$

It can be concluded from (10) that to minimize U_{RSC}, both $\boldsymbol{I}_{r2}^*$ and k_2 should be set as 0. The current reference can be obtained in the form of (11) (i.e., the form of demagnetizing current)

$$\boldsymbol{I}_r^* = k\boldsymbol{\psi}_{sn}(k < 0) \tag{11}$$

Consequently, the above analysis illustrates that by designing the current reference in the form of demagnetizing current after crowbar release, the unit can adapt to higher remaining EMF,

the operational period of crowbar can be decreased. However, in (11), the demagnetizing coefficient k is not determined. From (10) and (11), it is obvious that the amplitude of $\boldsymbol{I}_r^*$ and $\boldsymbol{U}_{\mathrm{RSC}}$ are simultaneously determined by k and the remaining stator natural flux, which will also affect the crowbar activation duration. Since the stator natural flux will continuously decay with time, to achieve the optimization of $\boldsymbol{I}_r^*$ and $\boldsymbol{U}_{\mathrm{RSC}}$, the demagnetizing coefficient k needs to be designed dynamically with the decay of the remaining stator natural flux.

B. Hybrid LVRT Control to Shorten Crowbar Operational Duration and Accelerate Reactive Response

In basic principle, only the dominant part of the EMF $\boldsymbol{E}_{rn}$ is considered. In this section, for accurate design, the positive-sequence component $\boldsymbol{E}_{rp}$ also needs to be considered. According to (8), when both $\boldsymbol{E}_{rp}$ and $\boldsymbol{E}_{rn}$ are in account, the required RSC output voltage $\boldsymbol{U}_{\mathrm{RSC}}$ to accurately track the current reference (11) can be expressed as

$$\begin{cases} \boldsymbol{U}_{\mathrm{RSC}} = \boldsymbol{U}_{rn} + \boldsymbol{U}_{rp} \\ \boldsymbol{U}_{rn} = \left(\frac{L_m}{L_s} + k\sigma L_r\right)\frac{d}{dt}\boldsymbol{\psi}_{sn}^r \\ \boldsymbol{U}_{rp} = \boldsymbol{E}_{rp} = \frac{L_m}{L_s} s\boldsymbol{U}_{sp}^r \end{cases} \tag{12}$$

where $\boldsymbol{U}_{rp}$ is the positive-sequence component of $\boldsymbol{U}_{\mathrm{RSC}}$, while $\boldsymbol{U}_{rn}$ is the natural component of $\boldsymbol{U}_{\mathrm{RSC}}$. $\boldsymbol{U}_{sp}$ is the positive-sequence component of the stator voltage.

Since the frequency of $\boldsymbol{\psi}_{sn}$ with respect to the rotor windings is ω_r, the amplitude of $\boldsymbol{U}_{\mathrm{RSC}}$ can be simplified and expressed as

$$U_{\mathrm{RSC}} \approx \left|\omega_r\left(\frac{L_m}{L_s} + k\sigma L_r\right)\right|\psi_{sn} + \left|\frac{L_m}{L_s} sU_{sp}\right| \tag{13}$$

From (11) and (13), the amplitudes of $\boldsymbol{I}_r^*$ and $\boldsymbol{U}_{\mathrm{RSC}}$ can be expressed by the demagnetizing coefficient k and the remaining stator natural flux. Based on the constraints of rotor current and voltage, the optimal value of demagnetizing coefficient k and the release condition of the crowbar can be obtained.

First, to protect the RSC, the amplitude of $\boldsymbol{I}_r^*$ (i.e., I_r^*) should not exceed the allowed maximum rotor current $I_{r\max}$. Thus, the demagnetizing coefficient should satisfy that

$$I_r^* = -k\psi_{sn} \le I_{r\max}(k < 0) \tag{14}$$

where $I_{r\max}$ is the allowed maximum rotor current, and is generally stated maximum of IGBT pulse current of 2 p.u.

From (14), It can be concluded that I_r^* is inversely proportional to the coefficient k. Thus, the minimum value of k can be expressed as

$$k_{\min} = -\frac{I_{r\max}}{\psi_{sn}} \tag{15}$$

Then, to release the crowbar, it is required to keep the system controllable, i.e., U_{RSC} should not exceed the RSC's maximum output voltage. It can be seen from (13), if $k\in(k_e,0)$, U_{RSC} is proportional to k and always less than E_r; if $k = k_e$, U_{RSC} is minimum; if $k < k_e$, U_{RSC} is inversely proportional to k. Where, k_e can be expressed as

$$k_e = -\frac{L_m}{L_s L_r - L_m^2} \tag{16}$$

Obviously, when $k\in(k_e,0)$, both U_{RSC} and I_r^* can be minimal, hence, it is the proper range for k. Moreover, in this range, I_r^* is inversely proportional to U_{RSC}. Therefore, U_{RSC} can be minimized when $I_r^* = I_{r\max}$. The coefficient $k_{\min}$ corresponding to the minimum U_{RSC}, which allows for the best system controllability while satisfying the current constraint, thus, it is the optimal value of k. Meanwhile, it can be seen from (15) that the value of $k_{\min}$ will be dynamically varied with ψ_{sn} decay during crowbar activation, which ensures that the system is always most conducive to release crowbar.

Substituting (15) into (13), the minimum U_{RSC} under current constraint can be expressed as $U_{R\min}$

$$U_{R\min} \approx \omega_r\frac{L_m}{L_s}\psi_{sn} - \omega_r\sigma L_r I_{r\max} + \left|\frac{L_m}{L_s} sU_{sp}\right| \tag{17}$$

When $U_{R\min}$ is less than the RSC's maximum output voltage, i.e., when (18) is satisfied, which means that the system could maintain controllability with remaining EMF at this time. Consequently, the crowbar release condition can be obtained as

$$U_{R\min} \approx \omega_r\frac{L_m}{L_s}\psi_{sn} - \omega_r\sigma L_r I_{r\max} + \left|\frac{L_m}{L_s} sU_{sp}\right| < U_{r\max} \tag{18}$$

where $U_{r\max}$ is the RSC's maximum output voltage, which can be approximated to the value of dc-bus voltage U_{dc}.

As the crowbar is released, the demagnetizing coefficient k should be fixed as the calculated optimum value $k_{\min}$ at the moment of crowbar release. In other words, the rotor current reference after crowbar release should be designed as

$$\boldsymbol{I}_r^* = k_{\mathrm{min}c}\boldsymbol{\psi}_{sn} = \frac{-I_{r\max}}{\boldsymbol{\psi}_{snc}}\boldsymbol{\psi}_{sn} \tag{19}$$

where $k_{\min c}$ and ψ_{snc} are fixed as the value of $k_{\min}$ and ψ_{sn} at the moment of crowbar release, respectively.

From (18) and (19), it can be concluded that through the dynamic demagnetizing coefficient design, I_r^* and U_{RSC} exactly satisfy the current constraint and voltage constraint of RSC at the moment of crowbar release, i.e., the RSC capacity is maximally utilized to resist the remaining EMF, thus, the crowbar activation time can be minimized.

In addition, after crowbar release, since the injection of demagnetizing current, the flux decay will be continuously accelerated. The demagnetizing current requirement will decrease and the RSC's current margin can be progressively utilized to inject additional positive-sequence current for reactive support. The RSC's current margin after crowbar release can be expressed as

$$I_m \approx I_{r\max} + k_{\mathrm{min}c}\boldsymbol{\psi}_{sn} \tag{20}$$

According to the German grid code [34], the reactive current required for output during the grid fault is shown in (21). Note that the reactive current is deduced based on the power invariant *abc*/*dq* transformation

$$I_Q = \frac{2K\left(0.9 - U_{sp}\right)L_s}{3U_{sp}L_m} - \frac{U_{sp}}{3\omega_s L_m}(K \ge 2) \tag{21}$$

Combining (20) and (21), in order to provide as much reactive current as possible under current constraint, the additional

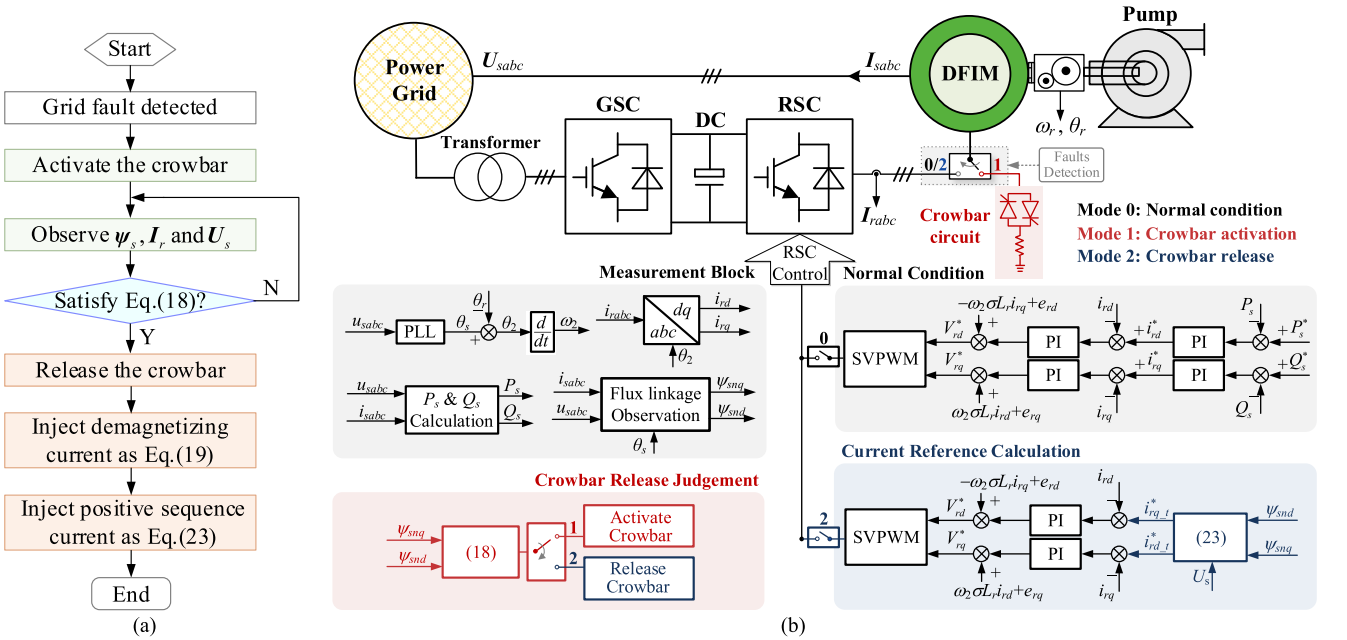

Fig. 8. System flowchart and control block diagram. (a) System flowchart. (b) Control block diagram.

positive sequence component added to the q-axis rotor current reference is commanded as

$$I_{rp1} = \max\{-I_m, -I_Q\} \tag{22}$$

Consequently, the corresponding flowchart and the overall control diagram of the proposed control is shown in Fig. 8. The operational sequence of the system would be as follows.

1) Under normal operating condition, the system operates in mode 0 (i.e., the classical *PQ* control is used).
2) Immediately upon detection of a grid fault activate the crowbar (i.e., the system operates in mode 1).
3) While the crowbar is active (i.e., under mode 1), observe the stator natural flux amplitude. Release the crowbar when the release condition given in (18) is satisfied, otherwise continue to activate the crowbar.
4) When the crowbar is released (i.e., the system operates in mode 2), activating the converter and starting to inject current according to (19), which can keep the system controllable and continue to accelerate the decay of the natural flux.
5) As the amplitude of natural flux decreases, the converter progressively introduces additional positive sequence current to supply reactive power according to (22). In this case, the unit operates in RPS mode, the current reference can be expressed as

$$\begin{cases} \boldsymbol{I}_{rd}^{*} = k_{\min c}\boldsymbol{\psi}_{snd} \\ \boldsymbol{I}_{rq}^{*} = k_{\min c}\boldsymbol{\psi}_{snq} + \boldsymbol{I}_{rp1} \end{cases} \tag{23}$$

C. Torque Characteristic and Reactive Support

To reduce the mechanical stress on unit during grid fault, the other important LVRT control objective is to eliminate the electromagnetic torque oscillation. Under symmetrical fault, the electromagnetic torque can be expressed as [35]

$$T_e = -\frac{3}{2}n_p\frac{L_m}{L_s}\left|\boldsymbol{\psi}_s \times \boldsymbol{I}_r\right| = -\frac{3}{2}n_p\frac{L_m}{L_s}\left|\left(\boldsymbol{\psi}_{sn}+\boldsymbol{\psi}_{sp}\right) \times \boldsymbol{I}_r\right| \tag{24}$$

where n_p is the number of pole pairs. $\boldsymbol{\psi}_{sp}$ is the positive-sequence component of stator flux.

According to (24), it is obvious that in order to suppress the torque oscillation to zero, the rotor current vector must be parallel to the stator flux vector. Therefore, to eliminate torque oscillation, the rotor current should include both the positive sequence component $\boldsymbol{I}_{rp}$ and the natural component $\boldsymbol{I}_{rn}$.

According to the method proposed in Section III–B, after crowbar release, the natural component in the current reference can be expressed as (19), i.e., $\boldsymbol{I}_{rn} = k_{\min c}\boldsymbol{\psi}_{sn}$; and when the reactive power support is provided, the positive sequence component in the current reference can be represented by (22). Obviously, $\boldsymbol{I}_{rp1} \neq k_{\min c}\boldsymbol{\psi}_{sp}$. Thus, the rotor current vector is not parallel to the stator flux, the RPS mode in Section III-B will induce torque oscillation. To suppress the torque oscillation, the additional positive sequence component needs to be modified.

Since the additional positive sequence component needs to be parallel to $\boldsymbol{\psi}_{sp}$, it can be expressed as $\boldsymbol{I}_{rp2} = k_p\boldsymbol{\psi}_{sp}$. Substituting it into (24), the electromagnetic torque can be derived as

$$T_e = -\frac{3}{2}n_p\frac{L_m}{L_s}\left|\boldsymbol{\psi}_{sn} \times \left(k_p - k_{\min c}\right)\boldsymbol{\psi}_{sp}\right| \tag{25}$$

According to (25), Obviously, as k_p approach $k_{\min c}$, the torque oscillation is reduced. Therefore, to suppress torque oscillation, $\boldsymbol{I}_{rp2}$ should be designed in the form of

$$I_{rp2} = \min\left\{I_m, k_{\min c}\psi_{sp}\right\} = \min\left\{I_m, -k_{\min c}\frac{U_{sp}}{\omega_s}\right\} \tag{26}$$

Obviously, the value of additional positive sequence component in (26) is positive, which results in the absorption of reactive

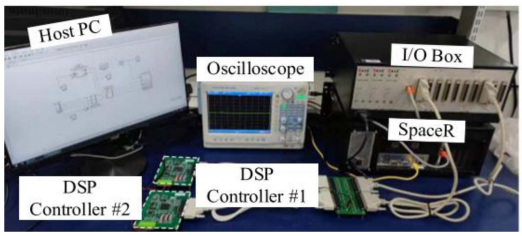

Fig. 9. Photograph of the HIL experimental setup.

power but effectively suppresses the torque oscillation. While, the additional positive sequence component in (22) is negative, which supports the grid but generates electromagnetic torque oscillation. It indicates that the control targets of reactive power support and torque oscillation suppression are conflicted, and should be designed according to practical needs.

Based on it, the modified method for suppressing torque oscillations can be obtained by replacing (23) in Fig. 8 with (27). In this case, the unit operates in torque oscillation suppression (TOS) mode

$$\begin{cases} \boldsymbol{I}_{rd}^{*} = k_{\mathrm{minc}}\boldsymbol{\psi}_{snd} \\ \boldsymbol{I}_{rq}^{*} = k_{\mathrm{minc}}\boldsymbol{\psi}_{snq} + \boldsymbol{I}_{rp2} \end{cases} \tag{27}$$

IV. Experimental Verification

To validate the effectiveness of the proposed method, a hardware-in-the-loop (HIL) experiment is performed. The experimental platform is shown in Fig. 9. The main circuits of VSPS and network are developed in a high-speed real-time simulator (SpaceR). There are two DSP controller executing the control algorithms, which exchange digital signals with the real-time simulator via the I/O box. Since the flux observation, calculation, data transmission and control are processed by the DSP in the HIL experiment, it provides more realism than simulation in verifying the system performance [36], [37].

The system parameters are listed in Table II in the Appendix. According to the rated dc-bus voltage, the RSC's maximum output voltage $U_{r\max}$ is 0.2 p.u. The allowed maximum rotor current $I_{r\max}$ is stated maximum of IGBT pulse current of 2.0 p.u. [39]. Note that GSC is the only responsible to maintain the dc-bus voltage, which plays a fundamental role for RSC controller. To reduce the complexity of the validation, the GSC's controller is omitted, and the dc-link voltage is assumed as constant.

In the experiment, the VSPS operates at the super synchronous speed (i.e., the slip $s = -0.1$). Under normal operating condition, the classical PQ control is used, and the control references of P_s and Q_s are set to 0.5 p.u. and 0, respectively. Under fault condition, an 80% three-phase grid voltage dip (i.e., $h = 0.8$) is selected for study. It is worth noting that the positive value of Q_s represents the provided reactive power to the grid.

Furthermore, a comparison among the three methods (i.e., the conventional crowbar control method [40], the improved crowbar control method in [29], and the proposed crowbar control method) is carried out. In the conventional crowbar control method, the crowbar is activated when the amplitude of rotor current I_r is greater than 2 p.u, and when I_r decreases to be less than 1.5 p.u, the crowbar will be released. In the crowbar control method proposed in [29], the crowbar is released when the amplitude of demagnetizing current $I_{rn} = -\psi_{sn}/(L_{ls}+L_{lr})$ decreases to less than 2 p.u, and then starting to inject the demagnetizing current and reactive current. The proposed strategy for comparison operates in RPS mode.

Figs. 10–17 show the experiment results of three crowbar control methods. The crowbar activation time corresponds to the time elapsed while the converter current was null. It can be observed that, all of methods can effectively suppress the rotor current within ± 2 p.u. However, there are some differences among these three crowbar control methods.

A. Crowbar Activation Time and Reactive Current Response

Fig. 10 shows the experimental results of the crowbar release condition and the crowbar activation time. It can be seen that, the crowbar activation time is the longest under the conventional crowbar control method, with an activation time of 191 ms. The method proposed in [29] effectively reduces the activation time of crowbar to 97 ms, but it is still not feasible to achieve the requirements of the grid codes for reactive power response speed. Under the method proposed in this article, the crowbar activation time is the shortest, which is only 33 ms. Compared with the conventional crowbar method and the method in [29], the proposed method reduces the crowbar activation time by 82% and 66%, respectively, which is able to achieve the requirements of most national grid codes.

Fig. 11 shows the experimental results of the dq-axis rotor current and reactive current reference. Fig. 12 shows the experimental results of the q-axis stator current injected into the grid, i.e., the reactive current injected into the grid from unit (reflecting the reactive power characteristics of the unit). From Fig. 11, it clearly shows that the reduction of the crowbar activation time allows a faster reactive current support control as well as a reduction of reactive power absorption. From Fig. 12, it can be seen that there are discrepancies in the reactive current characteristics (i.e., the value of reactive current) of the three methods during grid faults. The proposed method allows a positive average value of stator current during grid fault, which implies that reactive power can be generated during the entire LVRT period with the proposed method (RPS mode). With the other two control methods, the average value of stator current is negative, which means that the reactive current is absorbed for the first 200 ms after the grid fault occurs.

B. Rotor Voltage and Current Characteristics

Fig. 13 shows the experimental results of rotor voltage and current after crowbar release. Fig. 14 shows the experimental results of the dq-axis tracking error. It is obviously that after the release of the crowbar, the rotor current of all three methods is close to the maximum rotor current and contain natural components. However, the causes of the current characteristic are not the same.

Under the conventional crowbar control method, the rotor voltage is always maintained at 0.2 p.u. and saturated after the crowbar is released, while the current tracking error is the

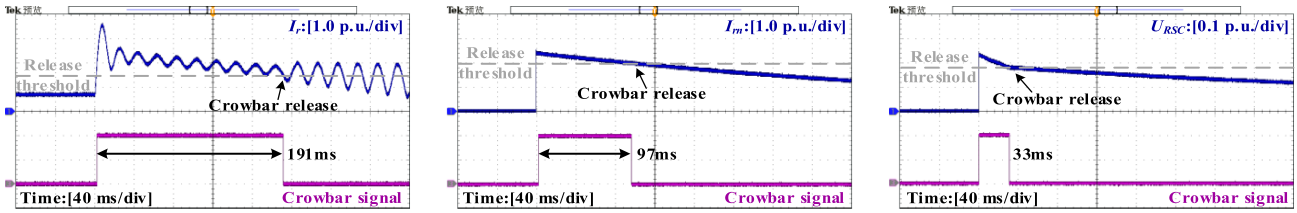

Fig. 10. Experimental results of crowbar signal. (a) Conventional crowbar control. (b) Crowbar control strategy proposed in [29]. (c) Crowbar control strategy proposed in this article (RPS mode).

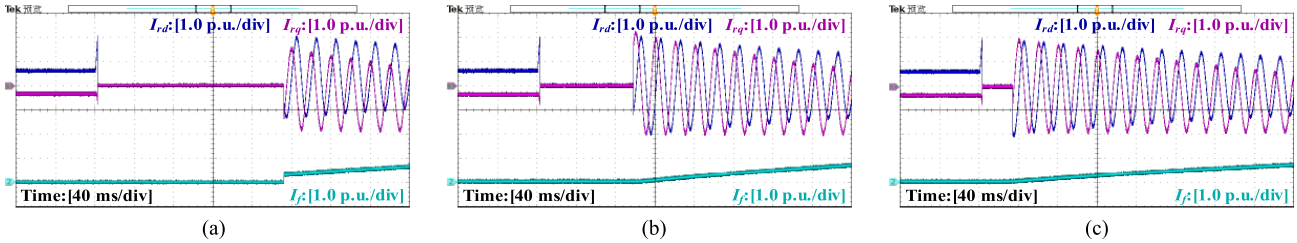

Fig. 11. Experimental results of the dq-axis rotor current and the injected reactive current. (a) Conventional crowbar control. (b) Crowbar control strategy proposed in [29]. (c) Crowbar control strategy proposed in this article (RPS mode). Note: I_f denotes the amplitude of the reactive current reference.

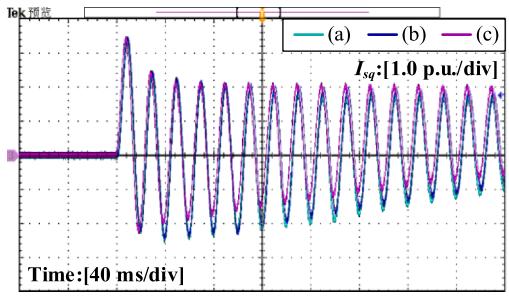

Fig. 12. Experimental results of the q-axis stator current. (a) Conventional crowbar control. (b) Crowbar control strategy proposed in [29]. (c) Crowbar control strategy proposed in this article (RPS mode).

largest and near 2 p.u. It indicates that the system cannot track the current reference, i.e., the system is out of control. In such situation, the rotor current is actually dominated by the current tracking error (i.e., the natural component of the rotor current). Since the amplitude of the current tracking error cannot be controlled, the uncontrolled rotor current is pernicious and tends to exceed the current limit, causing repeated activation of the crowbar.

Under the method in [29], it is obviously that the rotor voltage and the current tracking error are relatively small after the release of the crowbar. It indicates that the system has regained controllability. In such case, the rotor current reference can be designed to control the amplitude of the rotor current and the injection of reactive power, and there is no longer a risk of overcurrent. However, the utilization of the rotor voltage is poor with this method, leading to the crowbar activation time is relatively long.

Compared to the method in [29], the proposed method improves the utilization of the rotor voltage by dynamically designing the current reference. As a result, it reduces the time required for the system to regain controllability, shortening the activation time of the crowbar even further.

C. Flux Decay Characteristics

Fig. 15 shows the experimental results of the stator flux under the three methods. In general, the stator flux can be decayed in all three methods, but the process of decay are not the same. In the conventional method, the rapid decay of the stator natural flux is mainly during the crowbar activation time. Under the latter two methods, although the crowbar activation time is greatly reduced, the stator natural flux can still be decayed rapidly and controllably through RSC control after the crowbar release. Therefore, the latter two methods are more conducive to the continuous decay of the stator natural flux.

D. Electromagnetic Torque Characteristics

Fig. 15 shows the experimental results of the electromagnetic torque under the three methods. It can be seen that electromagnetic torque oscillations are still generated continuously after crowbar release in all methods, due to the injection of reactive current after crowbar release, as analyzed in Section II.

To validate the effectiveness of the proposed TOS mode control. The electromagnetic torque comparison among the three methods (i.e., the proposed TOS mode control, conventional crowbar control without additional reactive current, and control method in [29] without injecting additional reactive current) is carried out in Fig. 16.

Fig. 16 shows the experimental results of the electromagnetic torque under the above three methods. It can be seen that, under the proposed TOS mode control, the torque oscillation is significantly reduced at 33 ms due to the crowbar release. After

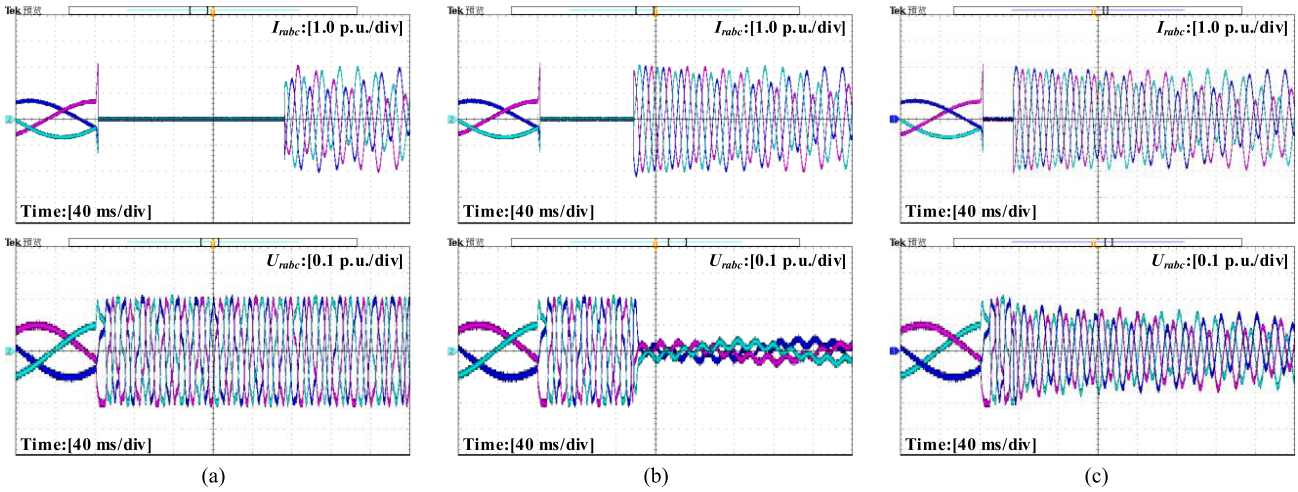

Fig. 13. Experimental results of rotor voltage and current. (a) Conventional crowbar control. (b) Crowbar control strategy proposed in [29]. (c) Crowbar control strategy proposed in this article (RPS mode).

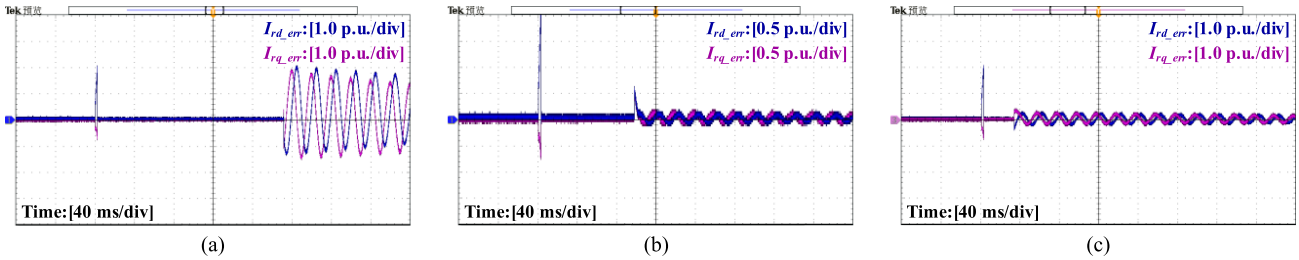

Fig. 14. Experimental results of dq-axis tracking error. (a) Conventional crowbar control. (b) Crowbar control strategy proposed in [29]. (c) Crowbar control strategy proposed in this article (RPS mode). Note: I_{rd_err} and I_{rq_err} denote the d-q axis current tracking error, respectively.

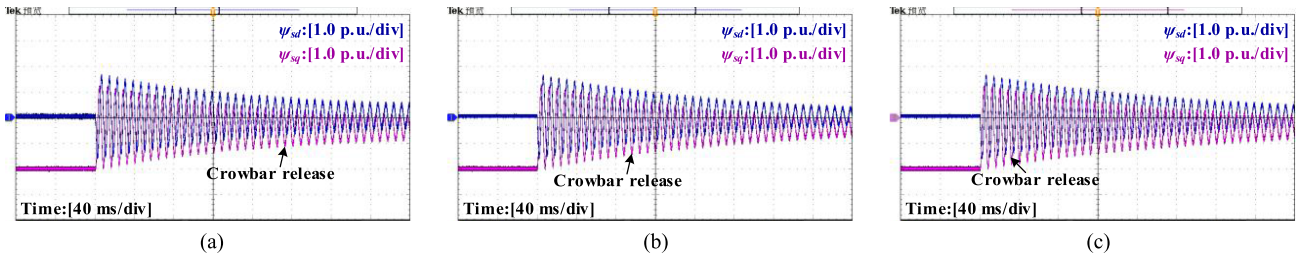

Fig. 15. Experimental results of stator flux. (a) Conventional crowbar control. (b) Crowbar control strategy proposed in [29]. (c) Crowbar control strategy proposed in this article (RPS mode).

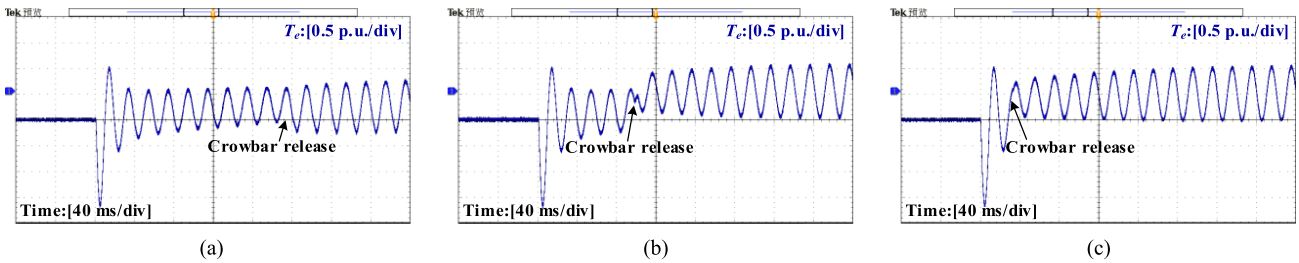

Fig. 16. Experimental results of electromagnetic torque. (a) Conventional crowbar control. (b) Crowbar control strategy proposed in [29]. (c) Crowbar control strategy proposed in this article (RPS mode).

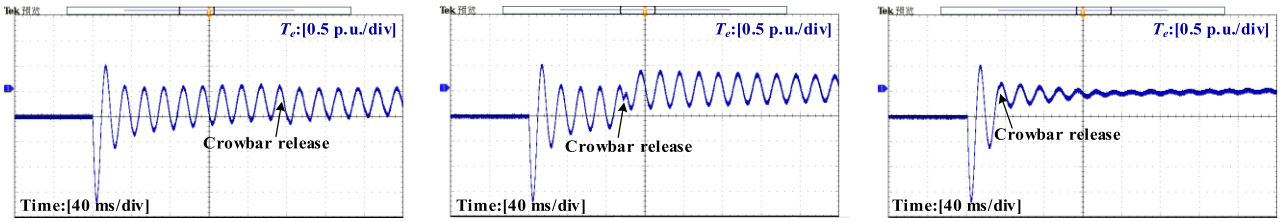

Fig. 17. Experimental results of the electromagnetic torque. (a) Conventional crowbar control. (b) Crowbar control strategy proposed in [29] without injecting additional reactive current. (c) Crowbar control strategy proposed in this article (TOS mode).

TABLE I
PERFORMANCE COMPARISON UNDER THREE CONTROL METHODS

Performance metrics	Conventional crowbar control	Crowbar control in [29]	Proposed Crowbar control
Crowbar activation time	191 ms	97 ms	33 ms
System controllability	★☆☆	★★★	★★★
Reactive current support	★☆☆	★★☆	★★★ (RPS mode)
Torque oscillation suppression	★☆☆	★★☆	★★★ (TOS mode)

crowbar release, the torque oscillation is gradually suppressed to 0 as the injected positive-sequence component increases. In the other two cases, the torque oscillations are consistently existed due to the rotor current not being parallel to the stator flux. Obviously, the proposed TOS mode control can effectively suppress the torque oscillation. It will extend the lifespan of drive trains.

Finally, to visually illustrate the system performance differences of the three methods, their performances are summarized in Table I. Therein, four key metrics are used: the crowbar activation time, the system controllability (reflected on the current tracking error), the reactive current support, and the torque oscillation suppression.

V. CONCLUSION

In this article, the crowbar release condition is analyzed from the perspective of system controllability, and a hybrid LVRT control of VSPS unit to shorten crowbar operational duration is proposed. The main conclusions can be summarized as follows.

1) The essential condition for releasing the crowbar is maintaining the controllability of VSPS unit under the undecayed EMF after crowbar release.
2) The controllability of the unit can be improved through injecting the demagnetizing current after crowbar release, thus shortening the operational period of the crowbar.
3) The crowbar operational duration can be minimized through optimizing the demagnetization coefficient dynamically, which fully utilize the RSC capacity to improve the unit controllability.
4) The transient control objectives of reactive power support and torque oscillation suppression can be achieved by modifying the additional positive-sequence component in the rotor current.

APPENDIX

TABLE II
SYSTEM PARAMETERS OF 300-MW VSPS

Parameter	Symbol	Value
Rated capacity	S_N	336 MVA
Rated power	P_N	300 MW
Rated stator voltage	U_N	15.75 kV
Rated frequency	f_n	50 Hz
Turn ratio	N_s/N_r	0.41
Stator resistance	R_s	0.002 p.u.
Stator leakage inductance	L_{ls}	0.14 p.u.
Magnetizing inductance	L_m	2.7 p.u.
Rotor resistance	R_r	0.003 p.u.
Rotor leakage inductance	L_{lr}	0.18 p.u.
Rated dc-bus voltage	U_{dc}	0.2 p.u.
Crowbar resistance value	R_c	0.1 p.u.

REFERENCES

[1] Y. Huang, W. Yang, and Z. Zhao, "Dynamic modeling and favorable speed command of variable-speed pumped-storage unit during power regulation," *Renewable Energy*, vol. 206, pp. 769–783, 2023.
[2] D. Zhu, Z. Wang, J. Hu, X. Zou, Y. Kang, and J. M. Guerrero, "Rethinking fault ride-through control of DFIG-based wind turbines from new perspective of rotor-port impedance characteristics," *IEEE Trans. Sustain. Energy*, vol. 15, no. 3, pp. 2050–2062, Jul. 2024.
[3] Y. Zheng, Q. Chen, D. Yan, and W Liu, "A two-stage numerical simulation framework for pumped-storage energy system," *Energy Convers. Manag.*, vol. 210, 2020, Art. no. 112676.
[4] J. D. Hunt and B. Zakeri, "Existing and new arrangements of pumped-hydro storage plants," *Renewable Sustain. Energy Rev.*, vol. 129, 2020, Art. no. 109914.
[5] M. Valavi and A. Nysveen, "Variable-speed operation of hydropower plants: A look at the past, present, and future," *IEEE Ind. Appl. Mag.*, vol. 24, no. 5, pp. 18–27, Sep./Oct. 2018.
[6] P. K. Steimer, O. Senturk, S. Aubert, and S. Linder, "Converter-fed synchronous machine for pumped hydro storage plants," in *Proc. IEEE Energy Convers. Congr. Expo.*, 2014, pp. 4561–4567.
[7] M. A. Bidgoli, W. Yang, and A Ahmadian, "DFIM versus synchronous machine for variable speed pumped storage hydropower plants: A comparative evaluation of technical performance," *Renewable Energy*, vol. 159, pp. 72–86, 2020.
[8] J. Schmidt, W. Kemmetmüller, and A. Kugi, "Modeling and static optimization of a variable speed pumped storage power plant," *Renewable Energy*, vol. 111, pp. 38–51, 2017.
[9] X. Tan, C. Li, and D. Liu, "Multi-time scale model reduction strategy of variable-speed pumped storage unit grid-connected system for small-signal oscillation stability analysis," *Renewable Energy*, vol. 211, pp. 985–1009, 2023.

[10] A. Joseph, K. Desingu, R. R. Semwal, T. R. Chelliah, and D. Khare, "Dynamic performance of pumping mode of 250MW variable speed hydro-generating unit subjected to power and control circuit faults," *IEEE Trans. Energy Convers.*, vol. 33, no. 1, pp. 430–441, Mar. 2018.
[11] D. Zhu, X. Zou, S. Zhou, W. Dong, Y. Kang, and J. Hu, "Feedforward current references control for DFIG-based wind turbine to improve transient control performance during grid faults," *IEEE Trans. Energy Convers.*, vol. 33, no. 2, pp. 670–681, Jun. 2018.
[12] H. Ye, "Variable-speed pumped hydro storage technology: Overview, solutions and case studies," in *Proc. 6nd Int. Conf. Power Renewable Energy*, 2021, pp. 1273–1278.
[13] A. Bocquel and J. Janning, "Analysis of a 300 MW variable speed drive for pump-storage plant applications," in *Proc. 11th Eur. Conf. Power Electron. Appl.*, 2005, pp. 1–10.
[14] R. Zhu, F. Deng, Z. Chen, and M. Liserre, "Enhanced control of DFIG wind turbine based on stator flux decay compensation," *IEEE Trans. Energy Convers.*, vol. 31, no. 4, pp. 1366–1376, Dec. 2016.
[15] M. Firouzi and G. B. Gharehpetian, "LVRT performance enhancement of DFIG-based wind farms by capacitive bridge-type fault current limiter," *IEEE Trans. Sustain. Energy*, vol. 9, no. 3, pp. 1118–1125, Jul. 2018.
[16] R. H. Yang and J. X. Jin, "Unified power quality conditioner with advanced dual control for performance improvement of DFIG-based wind farm," *IEEE Trans. Sustain. Energy*, vol. 12, no. 1, pp. 116–126, Jan. 2021.
[17] A. Joseph and T. R. Chelliah, "A review of power electronic converters for variable speed pumped storage plants: Configurations, operational challenges, and future scopes," *IEEE Trans. Emerg. Sel. Topics Power Electron.*, vol. 6, no. 1, pp. 103–119, Mar. 2018.
[18] M. A. Bidgoli, H. A. Mohammadpour, and S. M. T. Bathaee, "Advanced vector control design for DFIM-based hydropower storage for fault ride-through enhancement," *IEEE Trans. Energy Convers.*, vol. 30, no. 4, pp. 1449–1459, Dec. 2015.
[19] F. K. A. Lima, A. Luna, P. Rodriguez, E. H. Watanabe, and F. Blaabjerg, "Rotor voltage dynamics in the doubly fed induction generator during grid faults," *IEEE Trans. Power Electron.*, vol. 25, no. 1, pp. 118–130, Jan. 2010.
[20] S. Xiao, G. Yang, H. Zhou, and H. Geng, "An LVRT control strategy based on flux linkage tracking for DFIG-based WECS," *IEEE Trans. Ind. Electron.*, vol. 60, no. 7, pp. 2820–2832, Jul. 2013.
[21] L. Ran, D. Xiang, P. J. Tavner, and S. Yang, "Control of a doubly fed induction generator in a wind turbine during grid fault ride-through," *IEEE Trans. Energy Convers.*, vol. 21, no. 3, pp. 652–662, Sep. 2006.
[22] Y.-W. Shen, D.-P. Ke, W. Qiao, Y.-Z. Sun, D. S. Kirschen, and C. Wei, "Transient reconfiguration and coordinated control for power converters to enhance the LVRT of a DFIG wind turbine with an energy storage device," *IEEE Trans. Energy Convers.*, vol. 30, no. 4, pp. 1679–1690, Dec. 2015.
[23] S. Hu, X. Lin, Y. Kang, and X. Zou, "An improved low-voltage ride-through control strategy of doubly fed induction generator during grid faults," *IEEE Trans. Ind. Electron.*, vol. 26, no. 12, pp. 3653–3665, Dec. 2011.
[24] Q. Huang, X. Zou, D. Zhu, and Y. Kang, "Scaled current tracking control for doubly fed induction generator to ride-through serious grid faults," *IEEE Trans. Power Electron.*, vol. 31, no. 3, pp. 2150–2165, Mar. 2016.
[25] R. Zhu, Z. Chen, X. Wu, and F. Deng, "Virtual damping flux-based LVRT control for DFIG-based wind turbine," *IEEE Trans. Energy Convers.*, vol. 30, no. 2, pp. 714–725, Jun. 2015.
[26] D. Zhu, X. Zou, L. Deng, Q. Huang, S. Zhou, and Y. Kang, "Inductance-emulating control for DFIG-based wind turbine to ride-through grid faults," *IEEE Trans. Power Electron.*, vol. 32, no. 11, pp. 8514–8525, Nov. 2017.
[27] M. A. Bidgoli, H. A. Mohammadpour, and S. M. T. Bathaee, "Advanced vector control design for DFIM-based hydropower storage for fault ride-through enhancement," *IEEE Trans. Energy Convers.*, vol. 30, no. 4, pp. 1449–1459, Dec. 2015.
[28] A. Damdoum, I. Slama-Belkhodja, and M. Pietrzak-David, "Low voltage ride-through strategies for doubly fed induction machine pumped storage system under grid faults," *Renewable Energy*, vol. 95, pp. 248–262, 2016.
[29] J. Lopez, E. Gubia, E. Olea, J. Ruiz, and L. Marroyo, "Ride through of wind turbines with doubly fed induction generator under symmetrical voltage dips," *IEEE Trans. Ind. Electron.*, vol. 56, no. 10, pp. 4246–4254, Oct. 2009.
[30] K. Desingu, R. Selvaraj, T. R. Chelliah, and D. Khare, "Effective utilization of parallel-connected megawatt three-level back-to-back power converters in variable speed pumped storage units," *IEEE Trans. Ind. Appl.*, vol. 55, no. 6, pp. 6414–6426, Nov./Dec. 2019.
[31] Y. Chen, C. Deng, and Y. Zhao, "Coordination control between excitation and hydraulic system during mode conversion of variable speed pumped storage unit," *IEEE Trans. Power Electron.*, vol. 36, no. 9, pp. 10171–10185, Sep. 2021.
[32] J. B. Ekanayake, L. Holdsworth, X. Wu, and N. Jenkins, "Dynamic modeling of doubly fed induction generator wind turbines," *IEEE Trans. Power Syst.*, vol. 18, no. 2, pp. 803–809, May 2003.
[33] M. Tsili and S. Papathanassiou, "A review of grid code technical requirements for wind farms," *Int. Eng. Technol. Renewable Power Gener.*, vol. 3, no. 3, pp. 308–332, Sep. 2009.
[34] Tennet TSO GmbH, "Grid code—High and extra high voltage," 2012. [Online]. Available: https://goo.gl/z5Lepo
[35] G. Abad, J. Lopez, M. Rodriguez, L. Marroyo, and G. Iwanski, *Doubly Fed Induction Machine: Modeling and Control for Wind Energy Generation*. Hoboken, NJ, USA: Wiley, 2011.
[36] D. Zhu, X. Guo, B. Tang, J. Hu, X. Zou, and Y. Kang, "Feedforward frequency deviation control in PLL for fast inertial response of DFIG-based wind turbines," *IEEE Trans. Power Electron.*, vol. 39, no. 1, pp. 664–676, Jan. 2024.
[37] Y. Ma, D. Zhu, Z. Zhang, X. Zou, J. Hu, and Y. Kang, "Modeling and transient stability analysis for type-3 wind turbines using singular perturbation and Lyapunov methods," *IEEE Trans. Ind. Electron.*, vol. 70, no. 8, pp. 8075–8086, Aug. 2023.
[38] B. Hu, H. Nian, M. Li, Y. Liao, J. Yang, and H. Tong, "Impedance characteristic analysis and stability improvement method for DFIG system within PLL bandwidth based on different reference frames," *IEEE Trans. Ind. Electron.*, vol. 70, no. 1, pp. 532–543, Jan. 2023.
[39] G. Pannell, D. J. Atkinson, and B. Zahawi, "Minimum-threshold crowbar for a fault-ride-through grid-code-compliant DFIG wind turbine," *IEEE Trans. Energy Convers.*, vol. 25, no. 3, pp. 750–759, Sep. 2010.
[40] L. Peng, B. Francois, and Y. Li, "Improved crowbar control strategy of DFIG based wind turbines for grid fault ride-through," in *Proc. IEEE 24th Annu. Appl. Power Electron. Conf. Expo.*, 2009, pp. 1932–1938.

Donghai Zhu (Senior Member, IEEE) was born in Anhui, China, in 1992. He received the Ph.D. degree in electrical engineering from the Huazhong University of Science and Technology, Wuhan, China, in 2018.

He is currently an Associate Professor with the School of Electrical and Electronic Engineering, Huazhong University of Science and Technology, Wuhan, China. His current research interests include renewable power generation system and power electronic converters.

Dr. Zhu was selected for the National Postdoctoral Program for Innovative Talents in 2018. He was a recipient of IEEE TRANSACTIONS ON ENERGY CONVERSION Best Paper Award in 2019 and the Excellent Doctoral Dissertation Award of China Power Supply Society in 2022. He is currently an Associate Editor for IEEE TRANSACTIONS ON INDUSTRY APPLICATIONS, *IET Renewable Power Generation*, and *Protection and Control of Modern Power Systems*.

Zhen Wang was born in Anhui, China, in 1999. He received the B.S. degree in electrical engineering from Anhui University, Hefei, China, in 2021. He is currently working toward the M.S. degree in electrical engineering with the School of Electrical and Electronic Engineering, Huazhong University of Science and Technology, Wuhan, China.

His current research interests include doubly-fed variable speed pumped storage and low voltage ride-through.

Yumei Ma (Student Member, IEEE) was born in Shandong, China, in 1999. She received the B.S. degree in electrical engineering from Guizhou University, Guiyang, China, in 2020. She is currently working toward the Ph.D. degree in electrical engineering with the School of Electrical and Electronic Engineering, Huazhong University of Science and Technology, Wuhan, China.

Her current research interests include renewable energy generation systems, stability, and power quality of converter-based power systems.

Jiabing Hu (Senior Member, IEEE) received the B.Eng. and Ph.D. degrees in electrical engineering from the College of Electrical Engineering, Zhejiang University, Hangzhou, China, in 2004 and 2009, respectively.

From 2007 to 2008, he was funded by Chinese Scholarship Council as a visiting scholar with the Department of Electronic and Electrical Engineering, University of Strathclyde, Glasgow, U.K. From 2010 to 2011, he was a Postdoctoral Research Associate with Sheffield Siemens Wind Power research center and the Department of Electronic and Electrical Engineering, University of Sheffield, Sheffield, U.K. Since 2011, he has been a Professor with State Key Laboratory of Advanced Electromagnetic Engineering and Technology, and School of Electrical and Electronic Engineering, Huazhong University of Science and Technology, Wuhan, China. His current research interests include grid-integration of large-scale renewables, and modeling, analysis, and control of power electronized power systems.

Dr. Hu is an Editor of IEEE TRANSACTIONS ON ENERGY CONVERSIon, an Associate Editor of *IET Renewable Power Generation*, and a member of Editorial Board for Automation of Electric Power Systems. He is the co-convener of IEC SC8A JWG5 and an active expert of IEC SC8A WG1/AHG3. He was nominated in 2016, 2017, and 2018 by Elsevier to be between the 40 Most Cited Chinese Researchers in electrical and electronic engineering. He is the Fellow of Institute of Engineering and Technology.

Xudong Zou (Member, IEEE) was born in Hunan, China, in 1974. He received the B.S., M.S., and Ph.D. degrees in electrical engineering from the Huazhong University of Science and Technology, Wuhan, China, in 1997, 2000, and 2005, respectively.

Since 2005, he has been a Faculty Member with the Huazhong University of Science and Technology, where he is currently a Full Professor with the School of Electrical and Electronic Engineering. His current research interests include power electronic converters, renewable energy generation system, and flywheel energy storage.

Dr. Zou was a recipient of the IEEE TRANSACTIONS ON ENERGY CONVERSION Best Paper Award in 2019.

Yong Kang (Fellow, IEEE) was born in Hubei Province, China, in Oct. 16, 1965. He received the B.E., M.E., and Ph.D. degrees in electrical engineering from Huazhong University of Science and Technology, Wuhan, China, in 1988, 1991, and 1994, respectively.

In 1994, he was with Huazhong University of Science and Technology as a Lecturer and was promoted to Associate Professor in 1996 and to Full Professor in 1998. He has authored more than 60 technical papers. His research interests include power electronic converters, ac drivers, electromagnetic compatibility, and their digital control techniques, and WBG device packaging and applications.